Carbon-Binder Migration: A Three-Dimensional Evaporation Model for Lithium Ion Batteries

Teo Lombardo, [1,2] *Alain C. Ngandjong,* [1,2] *Amal Belhcen,* [1,2] *Mehdi Chouchane,*[1,2] *Abbos Shodiev,*[1,2] *Oier Arcelus,*[1,2] *Alejandro A. Franco* [1, 2, 3, 4, *]

[1] Laboratoire de Réactivité et Chimie des Solides (LRCS), UMR CNRS 7314, Université de Picardie Jules Verne, Hub de l'Energie, 15, rue Baudelocque, 80039 Amiens Cedex, France

[2] Réseau sur le Stockage Electrochimique de l'Energie (RS2E), FR CNRS 3459, Hub de l'Energie, 15, rue Baudelocque, 80039 Amiens Cedex, France

[3] ALISTORE-European Research Institute, FR CNRS 3104, Hub de l'Energie, 15, rue Baudelocque, 80039 Amiens Cedex, France

[4] Institut Universitaire de France, 103 Boulevard Saint Michel, 75005 Paris, France

* corresponding author: alejandro.franco@u-picardie.fr

ABSTRACT

Li-ion battery electrodes manufacturing is raising broad interest from both experimental and computational perspectives, due to its impact on the cost, mechanical and electrochemical properties of the final electrodes and cells. Among the different manufacturing steps, solvent evaporation can trigger heterogeneities along the electrode mesostructure through additives migration, which were found to affect significantly the final electrodes' properties. Despite acknowledging the importance of such heterogeneities, the drying step is often under evaluated at the experimental level, while the modelling community mainly adopts homogenized approaches. In this work, we present the first physics-based three-dimensional model able to mimic the additives migration occurring along the drying step, unlocking the generation of three-dimensional heterogeneous electrode mesostructures. We analyzed the effect of drying rate on the final electrode mesostructures, the dynamics of additives migration and how the developed heterogeneities affect the following manufacturing step, *i.e.* electrodes' compression. The results are in agreements with previous experimental findings and indicates trends not disclosed yet. Lastly, the implementation of complex drying procedures (three-stage drying) was tested and compared to its experimental counterpart.

KEYWORDS

Lithium-ion battery, evaporation, carbon-binder domain, electrode mesostructure, electrochemistry

1. INTRODUCTION

Li-ion battery (LIB) are being recognized as one of the key technologies of our time.[1–3] They can potentially unlock the widespread success of electric vehicles (EVs),[4–6] while assuring more flexible electric grids.[7] Nevertheless, high enough electrochemical performance and cycle life, as well as low cost, CO_2 footprint and a stable raw materials supply chain, are essential requisite to make sustainable the production upscale of LIBs. In this context, international actions underlining the importance of sustainable LIBs production, as the European[8] and global[9] battery alliance and the battery passport,[10] are particularly important. One way of improving LIBs performance and decreasing their cost is through novel materials. However, after three decades of commercial success of LIBs, the cathode's and anode's chemistries are rather similar to the ones commercialized in 1991 by Sony ($LiCoO_2$ | graphite), namely layered transition metal oxides (as $LiNi_xMn_yCo_zO_2$) cathodes and carbon-based anodes, respectively.[1] Then, an alternative pathway to enhance LIBs performance, cost and CO_2 footprint relies on optimizing composite electrodes, cells and battery packs manufacturing.[11–15] It has been estimated that the composite electrodes production alone account for ~40% of the battery cells production cost, and, in between them, >50% comes from slurry coating and solvent evaporation.[16] In another study, Schünemann *et al.*[17] found that coating and drying represent the main cost of electrode and cell manufacturing, except for the cost of materials.

Studying experimentally the evaporation process for high solid content (SC) dispersions, as LIBs slurries, requires specific equipment (which often need to be built *in house*) and clever strategies. The group of Professor Schabel[18–21] published a series of experimental works aiming to investigate the evaporation process in graphite-based anodes. In these studies, they demonstrated that: *(i)* high drying rate (HDR) leads to a gradient in binder distribution along the electrode thickness, lowering

electrode capacity and adhesion to the current collector. A strong binder-carbon affinity was also observed, suggesting that HDR could lead to a gradient in terms of carbon distribution as well; *(ii)* additives migration is not a linear process, it exists a specific time range in which it occurs; *(iii)* slurry drying is composed of two drying regimes, first the slurry film shrinks until reaching the final electrode thickness and then the pores start emptying until complete solvent evaporation. Both *(ii)* and *(iii)* were extensively demonstrated by them and other groups using adhesive measurements,[18] a devoted experimental set up to follow the solvent evaporation through fluorescent measurements[19] and by the development of a three-stage drying process,[21] upon others.[22,23]

On the one side, binder migration is today widely accepted by the battery community and it was previously observed through energy dispersive X-ray,[23–25] Raman[26] and Real-time fluorescent spectroscopy.[27] On the other side, the observation of light conductive additives migration is hampered by the presence of carbon in both binder and conductive phase, but it is supported by previous experimental observations for both LIBs cathodes and anodes.[18,23] The main reason of migration seems to be convective and capillary forces developed during drying, while diffusion tend to re-homogenize the system. Fast drying and additive migration is typically detrimental for the final electrochemical performance and battery cycle life,[28–30] promoting electrode cracking (particularly severe for the case of thick electrodes and water processing),[31,32] poorly interconnected heterogeneous electrode mesostructures[23,24] and poor adhesion to the current collector.[18,29]

From a computational perspective, the physical complexity of solvent evaporation in high SC dispersions makes challenging the development of devoted physics-based models. Most of the approaches used today for LIB slurry evaporation relies on 1-dimensional continuum models[22,33]

or 2-dimensional discrete models.[23,34] However, it was previously demonstrated by us[35–40] and others[41–44] the potential of 3-dimensional (3D) models explicitly considering the carbon-binder domain (CBD) phase together with the active material (AM) one, calling for 3D discrete evaporation models devoted to the case of LIBs.

To date, only two modelling approaches, considering both AM and CBD particles, were published for 3D LIB slurry evaporation: the one reported by us[35,37,38,40] and Forouzan *et al.*[45] and the one reported by Srivastava *et al.*[41] Both these approaches have been developed through the open-source molecular dynamics software LAMMPS.[46] Srivastava *et al.* considered the solvent implicitly by applying a Langevin[47] force field (FF) to the particles, while the evaporation was performed by simply shrinking the slurry structure until reaching the desired electrode thickness. Along our 3D manufacturing computational workflow,[35] the solvent at the slurry phase is accounted by expanding the CBD particles and decreasing their density. The latter makes the CBD at the slurry phase an effective particle enabling to account for carbon, binder and solvent, as extensively discussed by us in a previous work.[36] The evaporation is performed by shrinking the CBD diameter to remove all the solvent, leading to a particles rearrangement and to the dried electrode mesostructure. An advantage of such approach, respect the one of Srivastava *et al.*, is that the electrode macroproprierties (porosity, density, thickness) arises from the particles' interactions, rather than being imposed shrinking the simulation box. The latter allows comparing such macroscopic observables with their experimental counterpart in order to to parametrize the model, as previously showed.[35,45] However, none of the procedures discussed above could lead to heterogeneous electrode mesostructures. Bearing in mind the critical importance of additives migration and the economic interest of increasing the drying speed, it is of interest the development of 3D physics-based models able to simulate CBD migration during solvent evaporation.

The goal of this work is to propose a first physics-based 3D simulation workflow able to model CBD migration along the evaporation step, leading to heterogeneous electrode mesostructures. First, the model is presented and discussed in detail. Then, the impact of the evaporation rate on the simulated electrode mesostructures is discussed in terms of its structural features. Afterwards, we analyze how electrode compression (the typical step performed in LIB electrodes manufacturing after the drying) affects the heterogeneities developed along drying, and we assess the capability of the model to simulate complex drying procedures (three-stage drying). Lastly, an overview on the results obtained and the model perspectives are presented.

2. MODEL WORKFLOW

The workflow of the evaporation model proposed in this Article is schematized in Figure 1. This section will discuss the critical aspects of our modelling procedure, *i.e.*: *(i)* the slurry phase, *(ii)* the strategy used to model solvent removal and CBD migration, *(iii)* particles sedimentation, *(iv)* the consideration of the two drying regimes and *(v)* the FFs utilized.

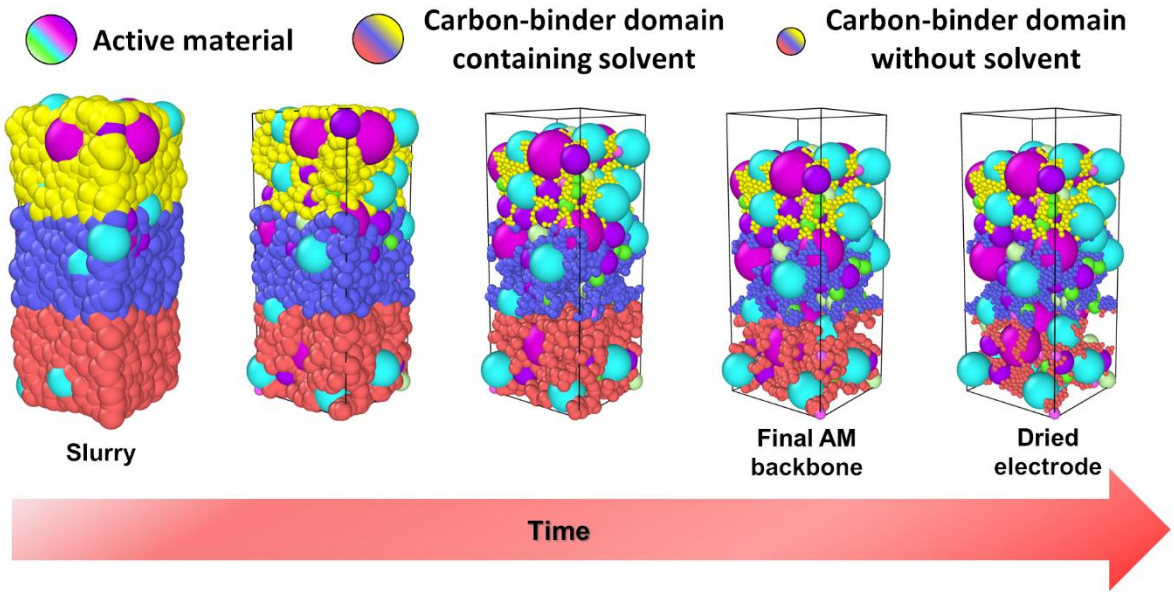

Figure 1. Schematic representation of the 3D drying models developed along this work.

The slurry phase has been previously validated by comparing the experimental and simulated slurry shear-viscosity curve, where the AM particle size distribution arises from devoted *in house* experimental measurements, while the CBDs are effective particles accounting for carbon, binder and solvent. Both AM and CBD particles are considered to be spherical. In the case study reported here, the slurry was composed of $LiNi_{0.33}Mn_{0.33}Co_{0.33}O_2$ (NMC), Carbon black (C65), polyvinylidene difluoride (PVdF) and N-Methyl-2-pyrrolidone (NMP). The weight ratio considered is 94:3:3 (NMC:C65:PVdF), with a SC of 65%. The SC is defined here as the mass of the solid components (NMC+C65+PVdF) divided to the total mass of the slurry (solid components + solvent). The validation of the simulated slurry structure utilized along this work is reported in section S1 of the Supplementary information.

As briefly presented in the introduction and as extensively discussed in our previous works,[35,40,48] the solvent removal is modelled by shrinking the CBD particles and increasing their density. Keeping in mind that evaporation is a surface phenomenon, it will more strongly affect the top of the slurry, while its bottom will be initially less affected. The key idea of the procedure proposed here is to module the speed of CBDs shrinking and density increase (*i.e.* the solvent removal in our computational workflow) as a function of their position. Particularly, CBD particles at the top of the slurry will shrink faster than the ones in the bottom. In this work, as illustrated in Figures 1 and 2A, the CBD particles are classified in three groups as a function of their z-coordinate along the slurry thickness: the ones in the first third (bottom, referred as CBD1), the ones in the second third (center, referred as CBD2) and the ones in the last third (top, referred as CBD3). Then, we defined the shrinking speed ($\mathbf{v}_{bottom}$) of CBD1 in such a way to remove all the solvent at the end of the simulation. In other terms, and considering that CBD1 particles are the ones with the slower shrinking speed, the latter means assuming that the solvent removal is complete at the end of the

drying process. Then, a relative shrinking factor (RSF) is defined for the center and top CBDs as $\mathbf{v}/\mathbf{v}_{bottom}$, where $\mathbf{v}$ is the shrinking speed for CBD2 and CBD3, respectively. Taking in mind that evaporation occurs faster in the top of the slurry respect to the bottom, both the RSFs are >1. Higher these RSFs, faster will be the solvent removal, indicating faster drying rates. For more details on how these different RSFs are implemented, the interest readers are referred to Section S2 of the Supplementary information.

Another important aspect that need to be considered along the drying process is particles sedimentation, which is leaded by gravity and atmospheric pressure. Gravity has been accounted by considering an extra acceleration term (equal to the gravitational acceleration) on each particle. Concerning the atmospheric pressure, LAMMPS allows applying a barostats[50] (*i.e.* controlling the pressure applied to the simulated system) only if all the boundary conditions are considered as periodic. Along this work, we considered x and y boundary conditions as periodic, while z is considered as not periodic to model consistently the drying step and additives migration. Therefore, the following computational strategy was used to account for atmospheric pressure: *(i)* the force acting on the whole slurry due to the atmosphere (F_{atm}) was calculated as the atmospheric pressure (P_{atm} = 101325 Pa) by the slurry surface (S_{slurry}) and *(ii)* a fraction of F_{atm} was added to each particle as a function of its surface area (S_i) normalized to the sum of surface areas of all the particles in the system. Then, through this strategy the sum of the forces applied to the particles in the system is consistently equal to F_{atm}. Considering all the above, sedimentation along the simulation is mainly driven by bigger and heavier AM particles, as expected experimentally. However, despite the positive results obtained through this rather simplistic strategy, it should be underlined that the development of barostat(s) applicable to the case of not periodic boundary conditions would be strongly beneficial to allow a finer tuning and control of the applied pressure,

as well as enabling a better generalizability of the model. Another possible approach would be the application of gravity only, which should be enough if simulating explicitly the drying time (typically in the order of minutes at the industrial scale and hours at the lab scale). However, the latter would have been prohibitively expensive by using the computational resources used along this work.

As discussed in the introduction, it has been previously observed that solvent evaporation is composed of two drying regimes, first the slurry shrinks until its final thickness (defining the final AM backbone) and then the pores start emptying.[20] In the computational procedure developed here, the final AM backbone was defined by freezing the AM particles when reaching a desired thickness (associated to a bulk porosity of ~46%) for all the evaporation rates considered. This strategy allows having approximately the same macro features (porosity, density, loading) for electrodes dried at different drying rate, enabling to focus on the only effect of evaporation rate on CBD migration and its impact on the electrode features. In addition, it should be stated here that an important aspect of our computational workflow is the implicit consideration of the nanoporosity of the (solid) CBD phase by volume expansion of the latter, as we discussed previously[35] and similarly to the approach of Srivastava *et al.*[41] Similarly to our previous works, here we considered a nanoporosity of ~50%, as found experimentally.[51] Along this manuscript, we will refer to "bulk" porosity when considering the pore phase only, while as "overall" porosity when accounting for the bulk pores + the CBD nanoporosity.

Lastly, the FFs used for the drying simulation are the same as the slurry one, namely Lennard-Jones (LJ), accounting for adhesive forces between particles, and granular Hertzian (GH), accounting for the mechanical properties of the system, as extensively discussed by us in previous studies.[35,36,40,48] However, the FFs parameters' value changes along the drying simulation, going

from the ones of the slurry (mimicking a liquid-like system) to the ones of the electrode (mimicking a solid system) through two linear regimes. Particularly, the two linear regimes link to the two drying regimes and the transition from the first to the second one occurs at the same time in which the AM particles are frozen. The parameters values used along this work are reported in Table S1 of the Supplementary information.

3. STRUCTURAL CHARACTERIZATION

The first and most important feature of the drying model developed here is its capability of mimicking the additives (here CBD) migration as a function of the DR. here, the DR was defined through the RSF applied to CBD2 (central region) and CBD3 (top region), *i.e.* the higher those values, the higher the DR. Figure 2A illustrates the 3D electrode mesostructures obtained at different DRs, with at their bottom the RSFs of the center (RSF_2) and top (RSF_3) CBD particles, reported as RSF_2 / RSF_3. The RSF of the CBD in the bottom (CBD1) is for definition kept constant to 1, as discussed in the previous Section. From these structures, it can be already observed that the higher the DR (from left to right), the higher the degree of heterogeneity, *i.e.* more CBDs particles in the top region of the electrode respect to its bottom. To quantify it, the evolution of CBD fraction for each region (CBD1, CBD2 and CBD3) along the drying is reported in Figure 2B for the 4 DRs considered. These results give us 3 main information: *(i)* the higher the DR, the higher the fraction of CBD3 at the expense of CBD2 and CBD1. *(ii)* the CBDs migration does not take place all along the drying, but rather in a specific time range. *(iii)* the time at which the CBDs migration starts and ends depends on the DR. Both *(i)* and *(ii)* have been found experimentally, as discussed along the Introduction, indicating that the model is capable of reproducing those trends.

To the best of our knowledge, *(iii)* was not previously reported, calling for further experimental studies aiming to verify and eventually quantify such phenomenon.

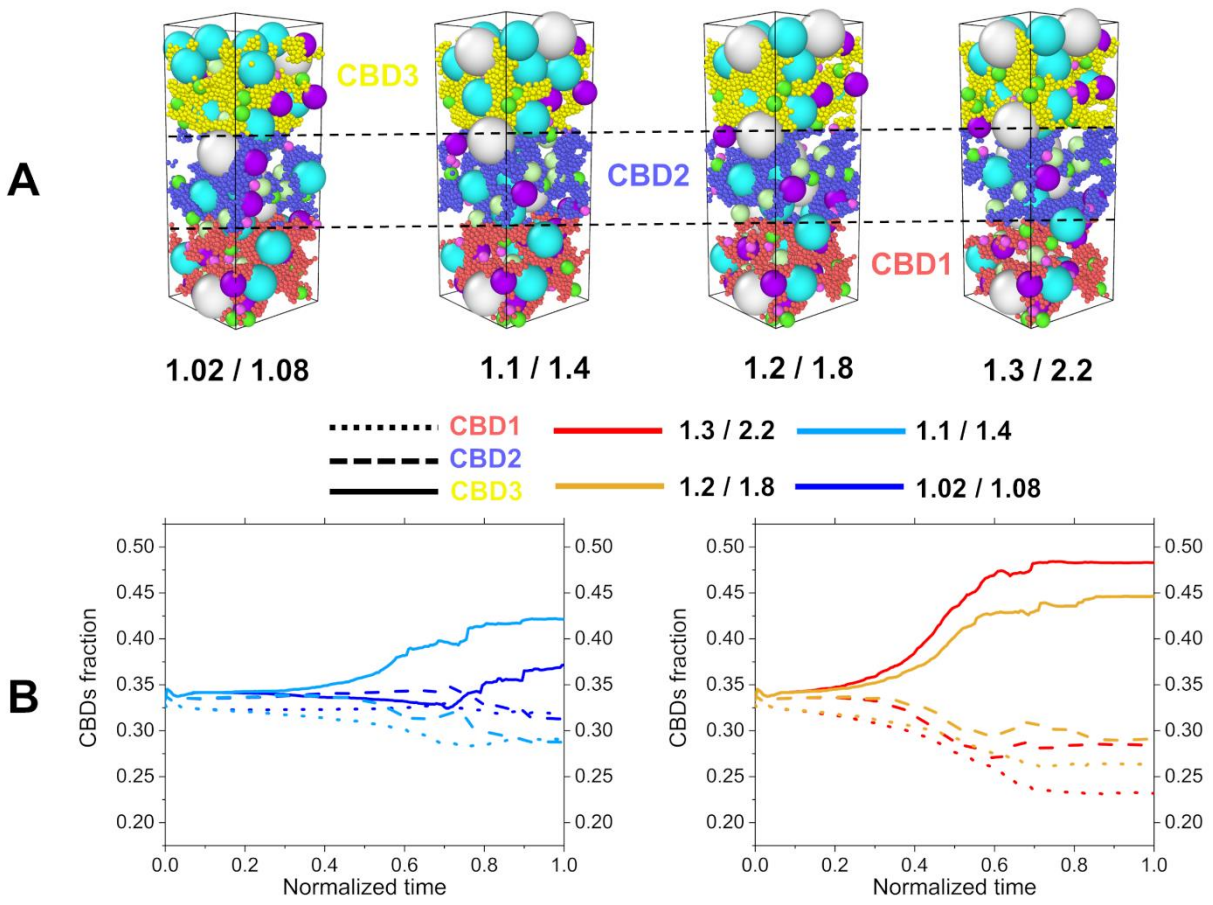

Figure 2. A) 3D rendering of 4 electrode mesostructures obtained from the same slurry but changing the drying conditions. The RSFs of CBD2 / CBD3 for each case is reported below the associated structure. The drying rate increases from left to right. The 4 electrodes have the same surface area (26.7 × 26.7 μm^2), an active loading of 13.6 mg cm^{-2}, a density of 2.24±0.01 and a bulk/overall porosity of 0.458±0.004 / 0.518±0.004. The errors reported here are the standard deviations, while bulk/overall porosity stand for the volume fraction of the bulk pore only and the bulk pore + 50% nanoporous CBD phase, respectively. **B)** Evolution of the fractions of CBD1 (dot line), CBD2 (dash line) and CBD3 (full line) during the drying. Here, cold colors indicate low/middle drying rates, while hot colors indicate middle/high drying rates. A normalized time of 0 indicates the slurry phase, while at 1 the drying is complete.

To further characterize the electrode mesostructures, the evolution of the different phase fractions (macro pores, CBD and AM) along the electrode thickness is reported in Figure 3. In terms of solid

phases (Figure 3 A), it is observable that the electrodes dried at lower DRs contain more AM in the first half of their thickness and lower in the second half, with respect to the ones dried at higher DRs. Lower DRs also leads to higher fraction of CBD in the bottom of the electrode and lower at its top when compared to higher DRs, while not significant differences can be observed for their central region. If the second trend was expected and already discussed (higher DR lead to lower/higher amount of CBD in the bottom/top region of the electrode), the first one is linked to the AM particles sedimentation. Faster solvent removal lead to reach more rapidly the transition between the first and the second drying regime, leaving less time to AM particles to sediment. In our model, it was found that the porosity defined as setpoint for switching from the first regime to the second one (where the final AM backbone is formed) was reached at normalized times of ~0.79 and ~0.62 for the lowest and highest DRs, respectively. The middle DRs (1.1 / 1.4 and 1.2 / 1.8) show intermediate transition times between these two. The latter means that the AM particles had ~27% more time to sediment when dried at the lowest DR with respect to the highest one, leading to higher concentration of this phase in the first part of the electrode. Concerning the pore phase (Figure 3B), it follows approximately the reverse trend respect the case of AM, indicating that the bulk porosity of the electrode is mainly controlled by the biggest particles' location.

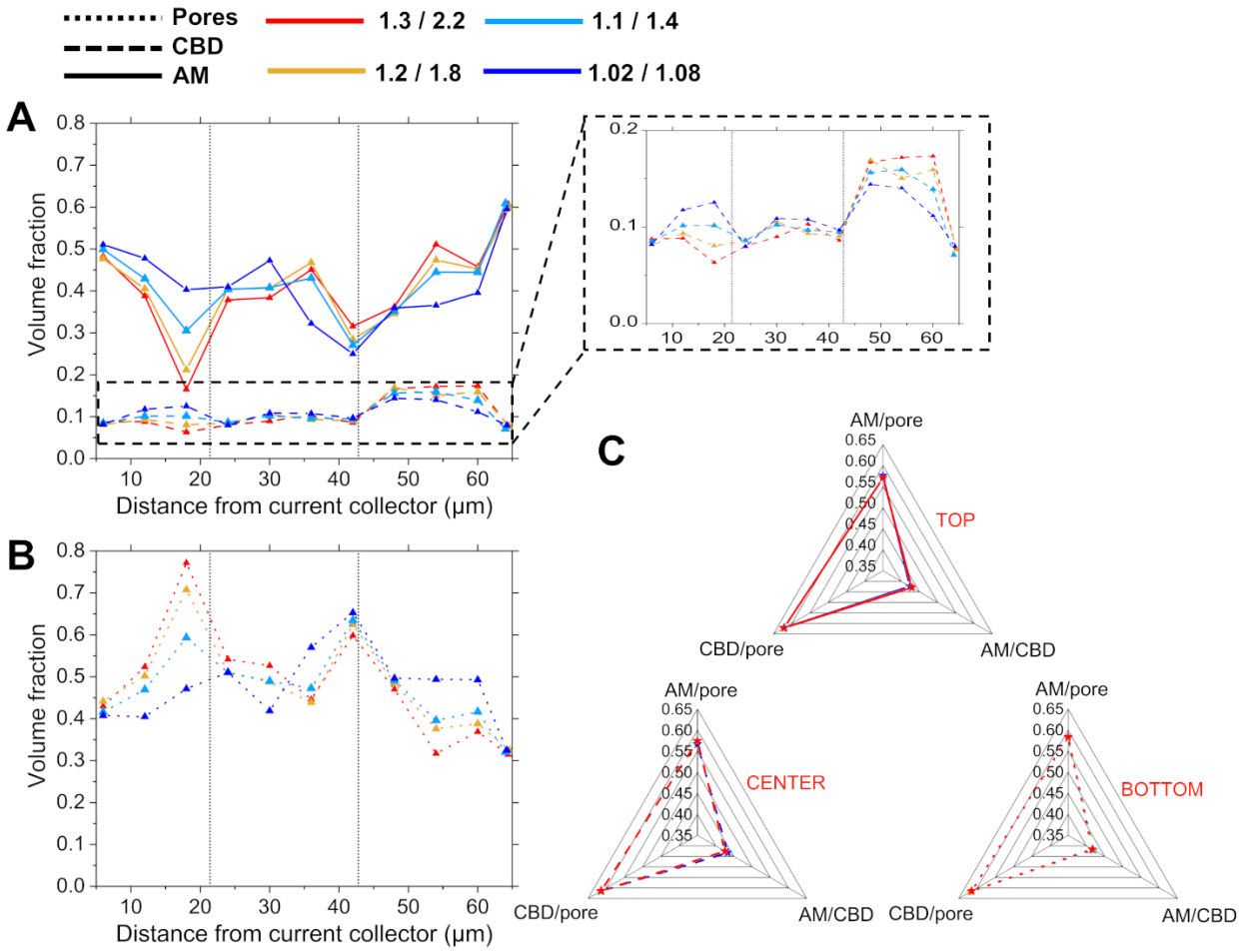

Figure 3. A) Evolution of AM, CBD and **B)** bulk pores volume fraction along the electrode thickness for electrodes dried at different DRs (Legend on the top left). The vertical dot lines indicate the 3 regions of the electrode defining the 3 different RSFs during the drying (Figure 2A). **C)** Percentage of AM surface in contact with pore (AM/pore) or CBD (AM/CBD) phases and percentage of CBD surface in contact with the pore phase (CBD/pore) for the same electrodes' regions (top, center and bottom) of A) and B). Here the top, center and bottom regions are indicated with full, dash and dot lines, respectively.

Besides the distribution of the AM, CBD and pore phase along the electrodes thickness, interfaces between the different phases is a key characteristic for electrochemical performance. Figure 3C

shows that the procedure employed along this work was capable of keeping substantially constant the percentage of AM surface in contact with both CBD and pores as well as the percentage of CBD surface in contact with the pore phase. The latter indicates that the application of different DRs, through the computational procedure proposed here, selectively affects the different phases' distribution (Figure 2 and 3 A and B), while the surface percentages are rather controlled by the FFs parameters' value used (here kept constant for the different structures).

Additionally, one could wonder if the heterogeneities developed along the drying step is kept along the next manufacturing steps (or not) and to which degree. Therefore, the 4 electrode mesostructures discussed above were compressed (mimicking the calendaring step) by reducing their thickness of 25%, reaching a bulk and overall porosities of 0.243±0.006 and 0.324±0.005, respectively. Figure 4 shows a schematic of how the electrode mesostructures evolve during compression (A), and the phases evolution of the calendered electrodes along their thickness (B). From B) two main aspects can be noticed: *i)* the differences between the electrode mesostructures are less pronounced respect the electrodes obtained after the drying (Figure 3), but some differences are still observable; *ii)* the compression reduces the volume fraction of the pore phase all along the electrode mesostructure, but in an asymmetric way, *i.e.* higher particles compaction (and then less pores) is observed in the top side of the electrode respect to its bottom. Point *ii)* is understandable considering that the compression is performed applying a plane at the top side of the electrode, which is moved down to mimic the rolls along calendering.[35,52] Therefore, the first particles that will feel the compression and that will be subsequently compacted are the ones in the electrodes' top layers. However, it should be mentioned that an aspect missing in the computational workflow used here is the role of roll's temperature, which is known to induce

higher deformability of the binder phase and that could play a role in its reorganization along the electrode.[53]

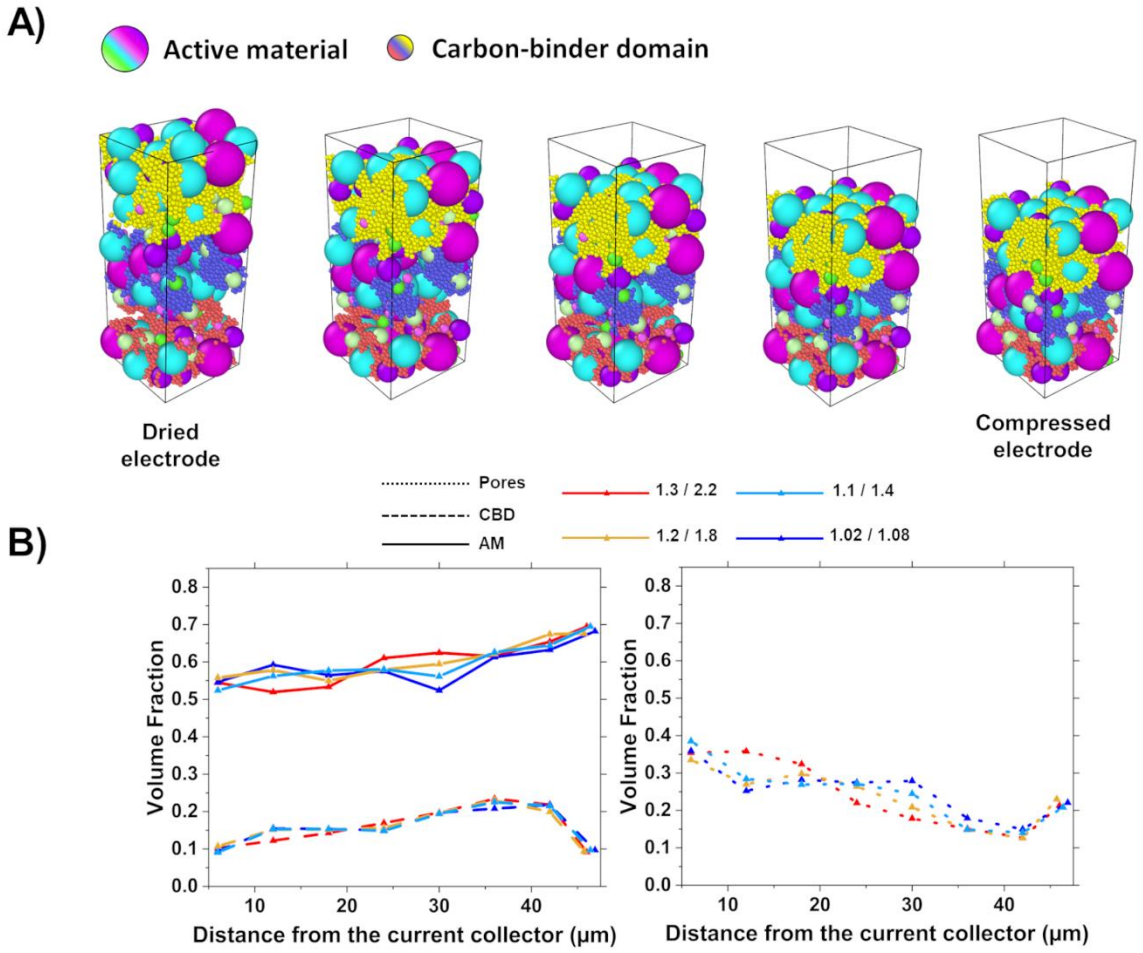

Figure 4. A) Evolution of the electrode mesostructures along compression for the case of the electrode 1.3 / 2.2. The different colors (red, blue and yellow) of the different CBD particles (indicating the 3 regions along the drying, Figure 2) are kept just as a guideline for the eyes, but all the CBD particles have the same physical properties along compression. **B)** Evolution of AM + CBD (left) and bulk pores (right) volume fraction along the electrode thickness.

Concerning point *i)*, for better evaluating the role of compression in leveling (but not completely removing) the heterogeneities of the dried electrodes, a direct comparison between dried and calendered electrodes is illustrated in Figure 5. Particularly, this figure reports the relative phases difference (RPD) for both compressed and dried (not compressed) electrodes along their thickness. The RPD is defined here as the ratio between the volume fraction of a (un)compressed electrode and the volume fraction of the (un)compressed one initially dried at the lowest DR (1.02 / 1.08). Therefore, the RPD offers a quantification of how different the analyzed electrode mesostructure is with respect to the less heterogeneous one (the closer the RPD to 1, the lower the differences). In addition, to easily compare compressed and not compressed electrodes, their associated RPD is reported as a function of their normalized thickness (0% stands for current collector side, 100% for separator side). From this analysis, it is possible to notice that the RPDs of the calendered electrodes (dash lines) are systematically lower compared to the not calendered ones (full lines), underling more clearly that the compression helps in leveling the heterogeneities arising from high evaporations rates. Lastly, comparing the RPDs for AM, CBD and pore phases for the different electrodes considered here (from left to right in Figure 5) underlines that the electrode mesostructures have a memory, meaning that the structure arising from one manufacturing step affects the following one. In the case study reported here, the latter reads as different calendered electrode mesostructures when applying the same compression procedure, but starting from electrodes dried differently.

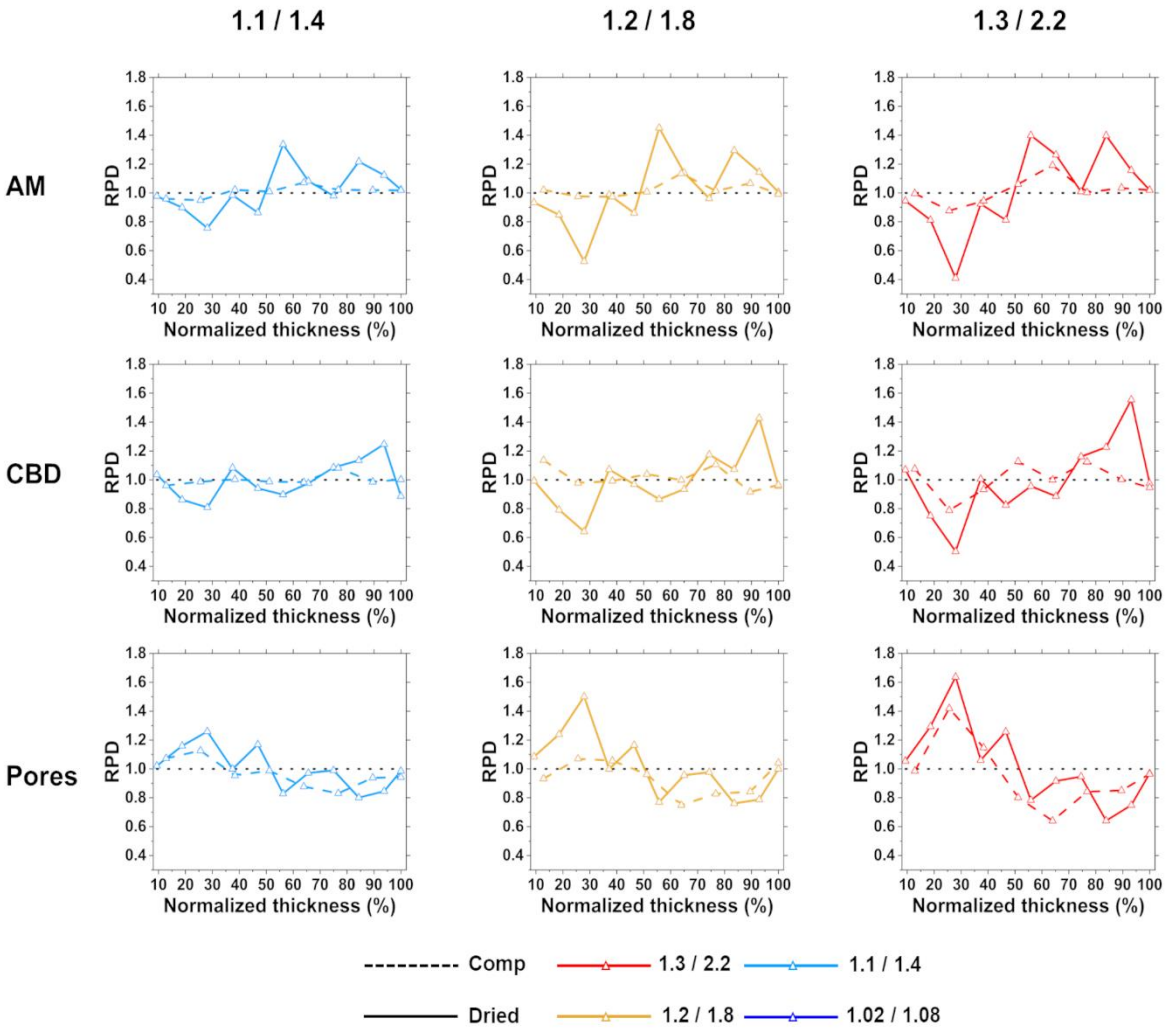

Figure 5. Evolution of the relative phases difference (RPD) for AM, CBD and (bulk) pore phases along their normalized thickness (0% stands for current collector side, 100% for separator side) for electrodes compressed (Compr) or not (Dried) that were dried at different DRs. The black dotted line is a guideline for the eyes indicating an RPD equal to 1.

4. THREE-STAGE DRYING

Another aspect to be tested of the model developed along this work is its capability of reproducing complex drying procedures. In particular, here we focused on the three-stage drying procedure proposed and developed by Jaiser *et al.*,[21] in which they applied an high DR at the

beginning and at the end of the drying procedure, while a low DR in between. Taking advantage of the additive migration occurring in a specific time range, this procedure allowed obtaining electrodes with the same properties of the ones dried at low DR while saving time (and then costs). In the following, we have applied the same logic for three different scenarios, *i.e.* setting a very low drying rate (1.02 / 1.03) at the beginning, mid or end of the drying procedure, while high DR (1.2 / 1.8) for the rest (Figure 6 A). Figure 6 B shows that applying LD rate at both the beginning and middle of the drying is beneficial in decreasing the CBD migration, being the second case the best condition, similarly to the scenario tested by Jaiser *et al*. On the contrary, applying a lower DR at the end of the drying is almost not effective in terms of reducing CBD migration, which is understandable considering that, at that stage in which LD rate is applied in such scenario, the majority of migration already occurred (Figure 2). All the above shows that the model can capture qualitatively the trend discussed by Jaiser *et al.*, while the quantitative results differ. Indeed, on the one hand they found that applying a LD rate in the middle of the drying allowed reaching the same structural properties (using adhesion with the current collector as metrics) of the electrode fully dried at LD rate. On the other hand, in our case such three-stage dried electrode is still more heterogeneous respect the one dried at 1.02 / 1.08 (figure 6 C), despite the use of a particularly low DR (1.02 / 1.03) in the three-stage scenario, indicating that there is still room for improvements of the model.

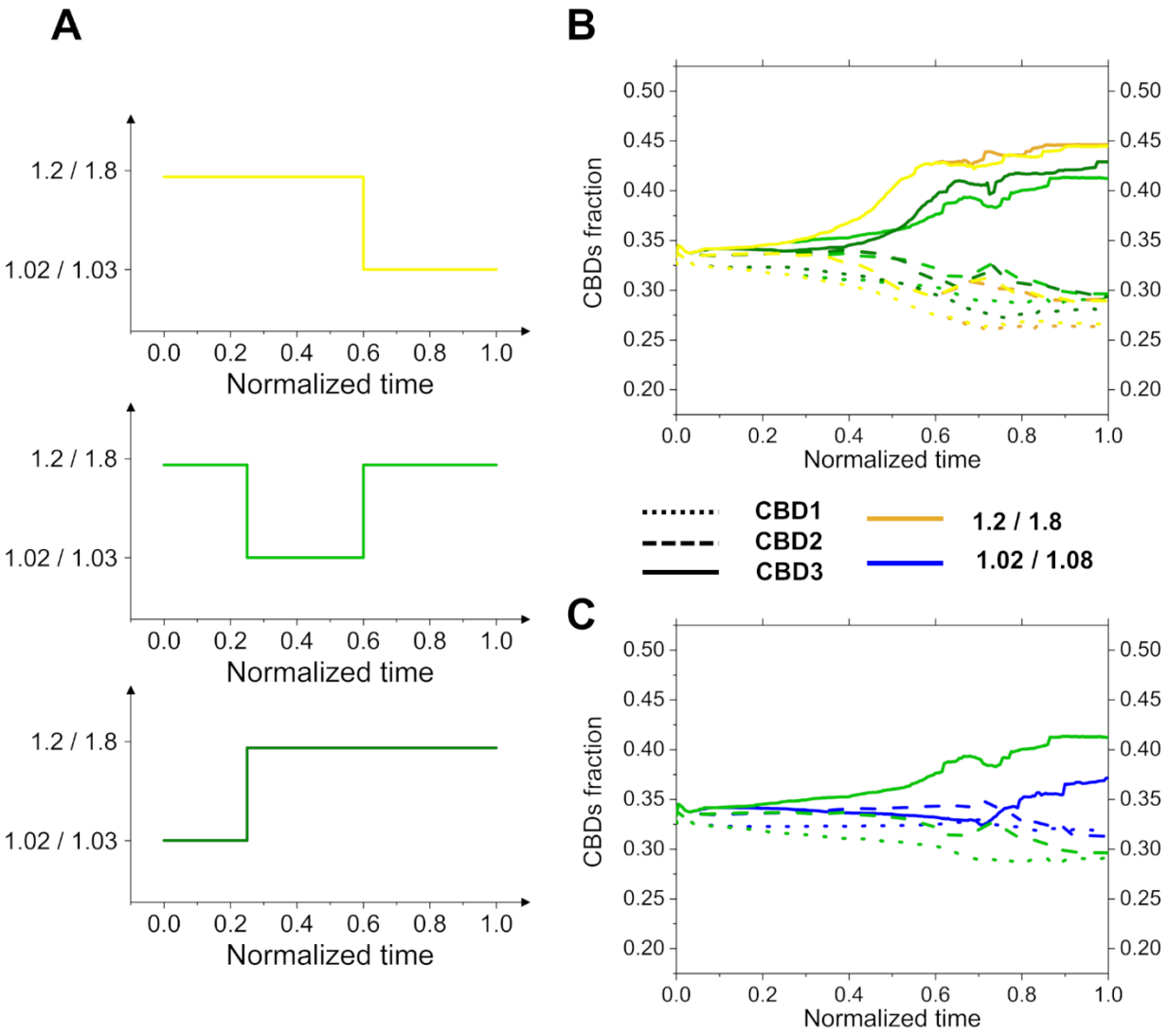

Figure 6. A) Schematic of the three-stage drying procedure implemented along this work, where the LD rate step was applied at the end (yellow), middle (light green) and beginning (dark green) of the drying. **B)** Comparison between the electrode fully dried at 1.2 / 1.8 and the ones dried with the three-stage drying procedure. **C)** Comparison of the less heterogeneous three-stage dried electrode and the one fully dried at 1.02 / 1.08.

5. CONCLUSIONS

In this work, we presented the first physics-based 3D model able to mimic solvent evaporation by explicitly considering additives migration for the case of NMC-based slurries and electrodes. The key idea that allowed to reach such result is to module the speed of transition from a liquid-like system (the slurry) to a solid one (the electrode) as a function of the slurry thickness (here divided into 3 zones), *i.e.* faster at the top respect its bottom. As a function of how fast this transition was in the top and middle regions respect the bottom one, different DRs were defined. By increasing the DR, a higher accumulation of the CBD phase in the electrodes' top region was found, linking to the additives migration and leading to heterogeneous electrodes' mesostructure. Particularly, it was observed that: *(i)* the higher the DR, the higher the fraction of CBD3 (top region) at the expense of CBD2 (middle region) and CBD1 (bottom region). *(ii)* the CBDs migration does not take place all along the drying, but rather in a specific time range. *(iii)* the time at which the CBDs migration starts and ends depends on the DR. *(i)* and *(ii)* are in agreements with previous experimental findings, while *(iii)* was not previously disclosed, calling for further studies in this direction. The electrodes dried at different DRs were then compressed of 25% respect their initial thickness, mimicking the calendering step. It was observed that this step induces a gradient in the electrodes' bulk pore phase (lower in its top compared to its bottom), due to the uniaxial compression applied from the top of the electrodes, while in the meantime levelling (but not completely removing) the electrodes' differences arising from the different DRs applied. The latter indicates once again at which degree the different manufacturing steps are interconnected, and that the final electrodes' properties arise from an interplay between them.

One last models' feature that was tested is its capability of reproducing three-stage drying procedures, which were found to be beneficial at the experimental level for reducing

manufacturing costs while keeping optimal electrodes' properties. The results obtained show that the model herein developed is able to capture qualitatively the trend disclosed experimentally, confirming that applying high DR at the beginning and end of the evaporation, while low DR in between, outputs less heterogeneous electrodes.

In terms of perspectives, the procedure described along this work should be tested for a wide range of electrodes' composition and AM particle size distribution to verify its generalizability to other scenarios with respect to the one considered here. In that sense, the code developed along this work will be released freely on the ARTISTIC project Github[54] for any computational researcher possibly interested into it, while it will be implemented in the ARTISTIC computational platform through a user-friendly interface.[49] The latter should allow experimentalists or not expert researchers to generate electrode mesostructures through the procedure discussed in this work, being free to select the desired electrode composition (weight ratio between AM and CBD), SC, AM particle size distribution and CBD size, which we hope could lead to a deeper testing of the model in a collaborative way. Lastly, we hope that this work can trigger the development of new 3D computational approaches focused on solvent evaporation or, more generally, 3D physics-based models able to generate heterogeneous electrodes mesostructures.

Computational section

The slurry and dried electrode simulations (155 AM particles and 5821 CBD particles) were performed through the open source molecular dynamics software LAMMPS took ~6 hours and ~6.5 days by using one and two node(s) (128 GB of RAM) composed of 2 processors (Intel® Xeon® CPU E5-2680 v4 @ 2.40GHz, 14 cores) on the MatriCs platform

(Université de Picardie-Jules Verne), respectively. The initial structure (prior the slurry equilibration) was generated to match the experimental composition and AM particles size distribution by locating randomly the AM and CBD particles in a simulation box big enough (200 × 200 × 500 μm, x × y × z) to avoid significant particles' overlap. All the details about the random structure generation can be found in the Supporting Information of Ref.[36] The slurry simulation was performed in a NPT environment, at 298 K and 1 atm, while the drying simulation was performed in a NVT environment at 353 K, while the pressure was considered as described in the Computational section. The boundary conditions of the slurry were considered as periodic in all the directions (x, y and z), while for the z direction two repulsive planes have been added at the bottom and top of the slurry structures to constrain the z direction, for which not periodic boundary conditions were applied. The slurry and drying simulations used a timestep of 1 and 0.1 ns, while the number of timestep was 13×10^6 and 100×10^6, respectively.

The compression was performed by keeping the same FFs parameters value of the dried electrode mesostructure (Table S1 in the Supplementary Information) and applying a moving plane to its top, which was moved down until reducing the electrode's thickness of 25% (with respect to its not-compressed state). This simulation was performed in LAMMPS and took approximately 20h by using one node (128 GB of RAM) composed of 2 processors (Intel® Xeon® CPU E5-2680 v4 @ 2.40GHz, 14 cores) on the MatriCs platform (Université de Picardie-Jules Verne).

The analysis of the volume fractions and surfaces percentage were performed through voxelization of the electrode mesostructures using a resolution of 0.1 μm.

Conflicts of interest

The authors declare that they have no known competing financial interests or personal relationships that could have influenced the work reported in this paper.

Acknowledgements

The authors acknowledge the European Union's Horizon 2020 research and innovation programme for the funding support through the European Research Council (grant agreement 772873, "ARTISTIC" project). A.A.F. acknowledges Institut Universitaire de France for the support. Results obtained using LAMMPS were achieved thanks to the MatriCS HPC platform from Université de Picardie-Jules Verne, particularly using the ARTISTIC project-dedicated computational nodes. The authors acknowledge Dr. Garima Shukla and Dr. Emiliano N. Primo from LRCS-Amiens (France) for very useful discussions.

Supplementary data

The supplementary Information.pdf file is available free of charge with this article, reporting the slurry phase validation, the FFs parameters' value used for the slurry, drying and calendaring simulation and some extra details on the computational procedure adopted to apply the different RSFs.

Data and code availability

The code developed along this work will be release freely on the ARTISTIC project Github[54] for any computational researcher possibly interested into it, while it will be implemented in the ARTISTIC computational platform through a user-friendly interface, which allows selecting the desired electrode composition (weight ratio between AM and CBD), SC, AM particle size distribution and CBD size.[49]

REFERENCES

(1) Winter, M.; Barnett, B.; Xu, K. Before Li Ion Batteries. *Chem. Rev.* **2018**, *118* (23), 11433–11456. https://doi.org/10.1021/acs.chemrev.8b00422.

(2) Blomgren, G. E. The Development and Future of Lithium Ion Batteries. *J. Electrochem. Soc.* **2017**, *164* (1), A5019–A5025. https://doi.org/10.1149/2.0251701jes.

(3) Larcher, D. & J.-M. T. Towards Greener and More Sustainable Batteries for Electrical Energy Storage. *Nat. Chem.* **2015**, *7* (January), 19–29. https://doi.org/10.1038/NCHEM.2085.

(4) Opitz, A.; Badami, P.; Shen, L.; Vignarooban, K.; Kannan, A. M. Can Li-Ion Batteries Be the Panacea for Automotive Applications? *Renew. Sustain. Energy Rev.* **2017**, *68*, *Part 1*, 685–692. https://doi.org/https://doi.org/10.1016/j.rser.2016.10.019.

(5) Ding, Y.; Cano, Z. P.; Yu, A.; Lu, J.; Chen, Z. Automotive Li-Ion Batteries: Current Status and Future Perspectives. *Electrochem. Energy Rev.* **2019**, *2* (1), 1–28. https://doi.org/10.1007/s41918-018-0022-z.

(6) Marinaro, M.; Bresser, D.; Beyer, E.; Faguy, P.; Hosoi, K.; Li, H.; Sakovica, J.; Amine, K.; Wohlfahrt-Mehrens, M.; Passerini, S. Bringing Forward the Development of Battery Cells for Automotive Applications: Perspective of R&D Activities in China, Japan, the EU and the USA. *J. Power Sources* **2020**, *459* (March), 228073. https://doi.org/10.1016/j.jpowsour.2020.228073.

(7) Dunn, B.; Kamath, H.; Tarascon, J. M. Electrical Energy Storage for the Grid: A Battery of Choices. *Science (80-.).* **2011**, *334* (6058), 928–935. https://doi.org/10.1126/science.1212741.

(8) https://ec.europa.eu/growth/industry/policy/european-battery-alliance_en (Accessed on February 2021).

(9) https://www.weforum.org/global-battery-alliance/home (Accessed on February 2021).

(10) https://batterypassport.org/ (Accessed on February 2021).

(11) Wood, D. L.; Li, J.; Daniel, C. Prospects for Reducing the Processing Cost of Lithium Ion Batteries. *J. Power Sources* **2015**, *275*, 234–242. https://doi.org/10.1016/j.jpowsour.2014.11.019.

(12) Ahmed, S.; Nelson, P. A.; Gallagher, K. G.; Susarla, N.; Dees, D. W. Cost and Energy Demand of Producing Nickel Manganese Cobalt Cathode Material for Lithium Ion Batteries. *J. Power Sources* **2017**, *342*, 733–740. https://doi.org/10.1016/j.jpowsour.2016.12.069.

(13) Turetskyy, A.; Thiede, S.; Thomitzek, M.; von Drachenfels, N.; Pape, T.; Herrmann, C. Toward Data-Driven Applications in Lithium-Ion Battery Cell Manufacturing. *Energy Technol.* **2020**, *8* (2), 1–11. https://doi.org/10.1002/ente.201900136.

(14) Günther, T.; Billot, N.; Schuster, J.; Schnell, J.; Spingler, F. B.; Gasteiger, H. A. The Manufacturing of Electrodes: Key Process for the Future Success of Lithium-Ion Batteries. *Adv. Mater. Res.* **2016**, *1140*, 304–311. https://doi.org/10.4028/www.scientific.net/amr.1140.304.

(15) Hawley, W. B.; Li, J. Electrode Manufacturing for Lithium-Ion Batteries—Analysis of Current and next Generation Processing. *J. Energy Storage* **2019**, *25* (July), 100862. https://doi.org/10.1016/j.est.2019.100862.

(16) *Boston Consulting Group Report "The Future of Battery Production for Electric Vehicles" Https://Www.Bcg.Com/Publications/2018/Future-Battery-Production-Electric-Vehicles (Accessed on September 2018)*.

(17) Schunemann, J.-H.; Dreger, H.; Bockholt, H.; Kwade, A. Smart Electrode Processing for Battery Cost Reduction. *ECS Trans.* **2016**, *73* (1), 153–159. https://doi.org/10.1149/07301.0153ecst.

(18) Jaiser, S.; Müller, M.; Baunach, M.; Bauer, W.; Scharfer, P.; Schabel, W. Investigation of Film Solidification and Binder Migration during Drying of Li-Ion Battery Anodes. *J. Power Sources* **2016**, *318*, 210–219. https://doi.org/10.1016/j.jpowsour.2016.04.018.

(19) Jaiser, S.; Funk, L.; Baunach, M.; Scharfer, P.; Schabel, W. Experimental Investigation into Battery

Electrode Surfaces: The Distribution of Liquid at the Surface and the Emptying of Pores during Drying. *J. Colloid Interface Sci.* **2017**, *494*, 22–31. https://doi.org/10.1016/j.jcis.2017.01.063.

(20) Kumberg, J.; Müller, M.; Diehm, R.; Spiegel, S.; Wachsmann, C.; Bauer, W.; Scharfer, P.; Schabel, W. Drying of Lithium-Ion Battery Anodes for Use in High-Energy Cells: Influence of Electrode Thickness on Drying Time, Adhesion, and Crack Formation. *Energy Technol.* **2019**, *7* (11), 1–11. https://doi.org/10.1002/ente.201900722.

(21) Jaiser, S.; Friske, A.; Baunach, M.; Scharfer, P.; Schabel, W. Development of a Three-Stage Drying Profile Based on Characteristic Drying Stages for Lithium-Ion Battery Anodes. *Dry. Technol.* **2017**, *35* (10), 1266–1275. https://doi.org/https://doi.org/10.1080/07373937.2016.1248975.

(22) Susarla, N.; Ahmed, S.; Dees, D. W. Modeling and Analysis of Solvent Removal during Li-Ion Battery Electrode Drying. *J. Power Sources* **2018**, *378* (December 2017), 660–670. https://doi.org/10.1016/j.jpowsour.2018.01.007.

(23) Stein, M.; Mistry, A.; Mukherjee, P. P. Mechanistic Understanding of the Role of Evaporation in Electrode Processing. *J. Electrochem. Soc.* **2017**, *164* (7), A1616–A1627. https://doi.org/10.1149/2.1271707jes.

(24) Kremer, L. S.; Hoffmann, A.; Danner, T.; Hein, S.; Prifling, B.; Westhoff, D.; Dreer, C.; Latz, A.; Schmidt, V.; Wohlfahrt-Mehrens, M. Manufacturing Process for Improved Ultra-Thick Cathodes in High-Energy Lithium-Ion Batteries. *Energy Technology*. 2020. https://doi.org/10.1002/ente.201900167.

(25) Jaiser, S.; Kumberg, J.; Klaver, J.; Urai, J. L.; Schabel, W.; Schmatz, J.; Scharfer, P. Microstructure Formation of Lithium-Ion Battery Electrodes during Drying – An Ex-Situ Study Using Cryogenic Broad Ion Beam Slope-Cutting and Scanning Electron Microscopy (Cryo-BIB-SEM). *J. Power Sources* **2017**, *345*, 97–107. https://doi.org/10.1016/j.jpowsour.2017.01.117.

(26) Hagiwara, H.; Suszynski, W. J.; Francis, L. F. A Raman Spectroscopic Method to Find Binder Distribution in Electrodes during Drying. *J. Coatings Technol. Res.* **2014**, *11* (1), 11–17. https://doi.org/10.1007/s11998-013-9509-z.

(27) Lim, S.; Ahn, K. H.; Yamamura, M. Latex Migration in Battery Slurries during Drying. *Langmuir* **2013**, *29* (26), 8233–8244. https://doi.org/10.1021/la4013685.

(28) Chen, Y. S.; Hu, C. C.; Li, Y. Y. Effects of Cathode Impedance on the Performances of Power-Oriented Lithium Ion Batteries. *J. Appl. Electrochem.* **2010**, *40* (2), 277–284. https://doi.org/10.1007/s10800-009-9971-6.

(29) Westphal, B.; Bockholt, H.; Gunther, T.; Haselrieder, W.; Kwade, A. Influence of Convective Drying Parameters on Electrode Performance and Physical Electrode Properties. *ECS Trans.* **2015**, *64* (22), 57–68. https://doi.org/10.1149/06422.0057ecst.

(30) Morasch, R.; Landesfeind, J.; Suthar, B.; Gasteiger, H. A. Detection of Binder Gradients Using Impedance Spectroscopy and Their Influence on the Tortuosity of Li-Ion Battery Graphite Electrodes. *J. Electrochem. Soc.* **2018**, *165* (14), A3459–A3467. https://doi.org/10.1149/2.1021814jes.

(31) Sahore, R.; Wood, D. L.; Kukay, A.; Grady, K. M.; Li, J.; Belharouak, I. Towards Understanding of Cracking during Drying of Thick Aqueous-Processed LiNi0.8Mn0.1Co0.1O2 Cathodes. *ACS Sustain. Chem. Eng.* **2020**, *8* (8), 3162–3169. https://doi.org/10.1021/acssuschemeng.9b06363.

(32) Lim, S.; Kim, S.; Ahn, K. H.; Lee, S. J. Stress Development of Li-Ion Battery Anode Slurries during the Drying Process. *Ind. Eng. Chem. Res.* **2015**, *54* (23), 6146–6155. https://doi.org/10.1021/acs.iecr.5b00878.

(33) Font, F.; Protas, B.; Richardson, G.; Foster, J. M. Binder Migration during Drying of Lithium-Ion Battery Electrodes: Modelling and Comparison to Experiment. *J. Power Sources* **2018**, *393*

(December 2017), 177–185. https://doi.org/10.1016/j.jpowsour.2018.04.097.

(34) Liu, Z.; Mukherjee, P. P. Microstructure Evolution in Lithium-Ion Battery Electrode Processing. *J. Electrochem. Soc.* **2014**, *161* (8), E3248–E3258. https://doi.org/10.1149/2.026408jes.

(35) Ngandjong, A. C.; Lombardo, T.; Primo, E. N.; Chouchane, M.; Shodiev, A.; Arcelus, O.; Franco, A. A. Investigating Electrode Calendering and Its Impact on Electrochemical Performance by Means of a New Discrete Element Method Model: Towards a Digital Twin of Li-Ion Battery Manufacturing. *J. Power Sources* **2021**, *485*, 229320. https://doi.org/10.1016/j.jpowsour.2020.229320.

(36) Lombardo, T.; Hoock, J.; Primo, E.; Ngandjong, C.; Duquesnoy, M.; Franco, A. A. Accelerated Optimization Methods for Force-Field Parametrization in Battery Electrode Manufacturing Modeling. *Batter. Supercaps* **2020**. https://doi.org/10.1002/batt.202000049.

(37) Chouchane, M.; Rucci, A.; Lombardo, T.; Ngandjong C., A.; Franco, A. A. Lithium Ion Battery Electrodes Predicted from Manufacturing Simulations: Assessing the Impact of the Carbon-Binder Spatial Location on the Electrochemical Performance. *J. Power Sources* **2019**. https://doi.org/https://doi.org/10.1016/j.jpowsour.2019.227285.

(38) Shodiev, A.; Primo, E. N.; Chouchane, M.; Lombardo, T.; Ngandjong, A. C.; Rucci, A.; Franco, A. A. 4D-Resolved Physical Model for Electrochemical Impedance Spectroscopy of Li(Ni1-x-YMnxCoy)O2-Based Cathodes in Symmetric Cells: Consequences in Tortuosity Calculations. *J. Power Sources* **2020**, *454*, 227871. https://doi.org/10.1016/j.jpowsour.2020.227871.

(39) Chouchane, M.; Primo, E. N.; Franco, A. A. Mesoscale Effects in the Extraction of the Solid-State Lithium Diffusion Coefficient Values of Battery Active Materials: Physical Insights from 3D Modeling. *J. Phys. Chem. Lett.* **2020**, *11*, 2775−2780.

(40) Ngandjong, A. C.; Rucci, A.; Maiza, M.; Shukla, G.; Vazquez-Arenas, J.; Franco, A. A. Multiscale

Simulation Platform Linking Lithium Ion Battery Electrode Fabrication Process with Performance at the Cell Level. *J. Phys. Chem. Lett.* **2017**, *8* (23), 5966–5972. https://doi.org/10.1021/acs.jpclett.7b02647.

(41) Srivastava, I.; Bolintineanu, D. S.; Lechman, J. B.; Scott, A. Controlling Binder Adhesion to Impact Electrode Mesostructure and Transport. *ACS Appl. Mater. Interfaces* **2020**. https://doi.org/10.1149/osf.io/ehdq6.

(42) Nguyen, T. T.; Villanova, J.; Su, Z.; Tucoulou, R.; Fleutot, B.; Delobel, B.; Delacourt, C.; Demortière, A. 3D Quantification of Microstructural Properties of LiNi0.5Mn0.3Co0.2O2 High-Energy Density Electrodes by X-Ray Holographic Nano-Tomography. *Adv. Energy Mater.* **2021**, *2003529*, 1–15. https://doi.org/10.1002/aenm.202003529.

(43) Lu, X.; Bertei, A.; Finegan, D. P.; Tan, C.; Daemi, S. R.; Weaving, J. S.; Regan, K. B. O.; Heenan, T. M. M.; Hinds, G.; Kendrick, E.; Brett, D. J. L.; Shearing, P. R. 3D Microstructure Design of Lithium-Ion Battery Electrodes Assisted by X-Ray Nano-Computed Tomography and Modelling. *Nat. Commun.* **2020**, *11* (2079), 1–13. https://doi.org/10.1038/s41467-020-15811-x.

(44) Lu, X.; Daemi, S. R.; Bertei, A.; Kok, M. D. R.; O'Regan, K. B.; Rasha, L.; Park, J.; Hinds, G.; Kendrick, E.; Brett, D. J. L.; Shearing, P. R. Microstructural Evolution of Battery Electrodes During Calendering. *Joule* **2020**, *4* (12), 2746–2768. https://doi.org/10.1016/j.joule.2020.10.010.

(45) Forouzan, M. M.; Chao, C. W.; Bustamante, D.; Mazzeo, B. A.; Wheeler, D. R. Experiment and Simulation of the Fabrication Process of Lithium-Ion Battery Cathodes for Determining Microstructure and Mechanical Properties. *J. Power Sources* **2016**, *312*, 172–183. https://doi.org/10.1016/j.jpowsour.2016.02.014.

(46) https://lammps.sandia.gov/ (Accessed on May 2021).

(47) https://lammps.sandia.gov/doc/fix_langevin.html (Accessed on February 2021).

(48) Rucci, A.; Ngandjong, A. C.; Primo, E. N.; Maiza, M.; Franco, A. A. Tracking Variabilities in the Simulation of Lithium Ion Battery Electrode Fabrication and Its Impact on Electrochemical Performance. *Electrochim. Acta* **2019**, *312*, 168–178. https://doi.org/https://doi.org/10.1016/j.electacta.2019.04.110.

(49) https://www.erc-artistic.eu/computational-portal (Accessed on June 2021).

(50) https://lammps.sandia.gov/doc/Howto_barostat.html (Accessed in May 2021).

(51) Zielke, L.; Hutzenlaub, T.; Wheeler, D. R.; Chao, C. W.; Manke, I.; Hilger, A.; Paust, N.; Zengerle, R.; Thiele, S. Three-Phase Multiscale Modeling of a LiCoO2 Cathode: Combining the Advantages of FIB-SEM Imaging and X-Ray Tomography. *Adv. Energy Mater.* **2015**, *5* (5), 1–8. https://doi.org/10.1002/aenm.201401612.

(52) Sangrós Giménez, C.; Finke, B.; Schilde, C.; Froböse, L.; Kwade, A. Numerical Simulation of the Behavior of Lithium-Ion Battery Electrodes during the Calendaring Process via the Discrete Element Method. *Powder Technol.* **2019**, *349*, 1–11. https://doi.org/10.1016/j.powtec.2019.03.020.

(53) Chen, H.; Ling, M.; Hencz, L.; Ling, H. Y.; Li, G.; Lin, Z.; Liu, G.; Zhang, S. Exploring Chemical, Mechanical, and Electrical Functionalities of Binders for Advanced Energy-Storage Devices. *Chem. Rev.* **2018**, *118* (18), 8936–8982. https://doi.org/10.1021/acs.chemrev.8b00241.

(54) https://github.com/ARTISTIC-ERC/Manufacturing-Model-Codes (accessed on June 2021).